ADVANCED FUNCTIONAL MATERIALS
www.afm-journal.de

'Oxygen Bound to Magnesium' as High Voltage Redox Center Causes Sloping of the Potential Profile in Mg-Doped Layered Oxides for Na-Ion Batteries

Yongchun Li, Konstantin Köster, Katherine A. Mazzio, Yanan Sun, Annica I. Freytag, Deniz Wong, Christian Schulz, Götz Schuck, Volodymyr Baran, Alba San Jose Mendez, Marcin Zając, Payam Kaghazchi, and Philipp Adelhelm**

>The potential profile of layered oxides as cathodes for Na-ion batteries can be well tuned by cation doping. Doping typically leads to changes in the phase behavior and the redox chemistry, but the underlying mechanisms remain poorly understood, especially at potentials above ≈4 V vs. Na^+/Na. Here, the influence of Mg-doping on the properties of layered O3-$NaNi_{0.5}Mn_{0.5}O_2$ is studied by means of synchrotron methods (XAS, RIXS, operando XRD) and DFT calculations. A strong oxygen redox activity is observed at high voltages, and Mg is found to induce an OP2 phase at low concentration (10%) and a solid solution type reaction at a high concentration (25%), thus greatly enhancing the cycle life. The change toward a more sloping charge profile with increasing Mg content is caused by a new redox center (arising from the 'O bound to Mg') having a higher redox potential but being more irreversible compared to the redox activity of 'O bound to Ni'. The appearance of an additional redox center explains findings obtained for other doped Ni- and Mn-based layered oxides, which also show a sloping potential in the high voltage region.

1. Introduction

Sodium-ion batteries (SIBs) are currently being commercialized and are seen as a promising energy storage technology based on more abundant, non-critical elements while achieving energy densities close to those of Li-ion batteries (LIBs).[1–3] A straight-forward approach for increasing the energy density of SIBs with layered oxides as cathode active materials (CAMs) is to increase the charging cut-off voltage.[4] Extending the upper cutoff potential beyond 4 V vs. Na^+/Na will, therefore in most cases result in a significantly higher storage capacity and hence higher average voltage and energy density.[5–7] However, too high a charging voltage causes poor cycle life due to degradation of the electrode materials and/or electrolyte decomposition.[8] To overcome these issues, a fundamental

Y. Li, K. A. Mazzio, Y. Sun, A. I. Freytag, P. Adelhelm
Humboldt-University Berlin
Brook-Taylor-Str. 2, 12489 Berlin, Germany
E-mail: philipp.adelhelm@hu-berlin.de

K. A. Mazzio, Y. Sun, A. I. Freytag, D. Wong, C. Schulz, G. Schuck, P. Adelhelm
Helmholtz-Zentrum Berlin für Materialien und Energie GmbH
Hahn-Meitner-Platz 1, 14109 Berlin, Germany

K. Köster, P. Kaghazchi
Forschungszentrum Jülich GmbH
Institute of Energy Materials and Devices - Materials Synthesis and Processing (IMD-2)
52425 Jülich, Germany
E-mail: p.kaghazchi@fz-juelich.de

The ORCID identification number(s) for the author(s) of this article can be found under https://doi.org/10.1002/adfm.202519132

DOI: 10.1002/adfm.202519132

V. Baran, A. S. J. Mendez
Deutsches Elektronen-Synchrotron (DESY)
Notkestraße 85, 22607 Hamburg, Germany

K. Köster, P. Kaghazchi
MESA+ Institute for Nanotechnology
University of Twente
Enschede 7500 AE, The Netherlands

M. Zając
National Synchrotron Radiation Centre SOLARIS
Czerwone Maki 98, Kraków 30-392, Poland

K. A. Mazzio
Institute of Chemical Technologies and Analytics
TU Wien
Getreidemarkt 9, Vienna 1060, Austria

K. A. Mazzio
X-Ray Center
TU Wien
Lehargasse 4, Vienna 1060, Austria

understanding of the degradation mechanism of cathode materials at high voltages (above 4.0 V vs Na^+/Na) is essential.

Layered transition metal oxides (Na_xTMO_2, where TM is a transition metal and x indicates the amount of Na per formula unit) are one of the most important classes of cathode materials for SIBs due to their compositional variety and their ability to provide high redox potentials combined with high capacities.[1,4,9–12] In addition, previous studies have suggested that oxygen may also be actively involved in the electrochemical reaction between many layered oxides at high voltages, further improving the practical electrode capacity.[13–17] Among the layered oxides, Ni-containing layered oxides for SIBs have attracted significant attention due to their high operating voltages and large capacities. In particular, $NaNi_{0.5}Mn_{0.5}O_2$, referred to as the O3 phase according to Delmas' notation, is attractive since it has a specific capacity of more than 200 mAh g^{-1} at a cut off voltage above 4.2 V.[4,18,19] However, when charged to high voltages (deep desodiation), complex phase transitions occur that include a sudden reduction in the *c* lattice parameter of over 20%. This behavior has been correlated with accelerated degradation of the material.[18,20]

To mitigate the degradation of O3-$NaNi_{0.5}Mn_{0.5}O_2$ at high voltages, many cations have been used as substitutional elements for Ni, including Li^+, Mg^{2+}, Al^{3+}, Zn^{2+}, Zr^{4+}, Sn^{4+}, etc. (with typical amounts of 2-10% with respect to the total amount of transition metals per formula unit).[20–27] Interestingly, two distinctly different behaviors have been reported at high voltage. Substitution of Ni with Mg^{2+}, Zn^{2+}, Cu^{2+}, and Li^+ can suppress the high voltage plateau and induce a sloping potential profile for the material.[21,22,28,29] Meanwhile, doping with Zr^{4+} and Sn^{4+} have been observed to preserve the high voltage plateau of the material.[25,27] It is worth noting that sloping potential profiles may provide an increase in average voltage compared to potential profiles showing similar capacities but based on plateaus, see Figure S1 (Supporting Information). A sloping potential profile in these types of materials has typically been explained by suppression of the O3 to P3 phase transition above 4.0 V.[30,31] However, the situation is more complex as there is always a combined effect of the dopant on the redox behavior and on the structural evolution. Moreover, the behavior can also change depending on the amount of dopant that is added, as recently shown for Mg doping in P2-$Na_{0.67}Ni_{0.33}Mn_{0.67}O_2$.[32] Therefore, there is a great need to better understand the role of dopants on layered oxides in the high voltage region with the aim of mitigating aging mechanisms.

In this work, we choose Mg to substitute Ni sites to study its impacts on the structural evolution, redox activities, and electrochemical behaviors of O3-$NaNi_{0.5}Mn_{0.5}O_2$, especially in the high voltage region (above 4.0 V). Similar to our previous observations on the Mg doped P2-$Na_{0.67}Ni_{0.33}Mn_{0.67}O_2$, the dopant is found to induce a sloping potential profile, which becomes more sloping as the doping content increases. Through synchrotron-based *operando* XRD, it is found that doping suppresses the formation of the intermediate phase (O'3), delays the occurrence of the phase transition below 4.0 V, and induces distinct structural behaviors at high voltage: a reversible OP2 phase at 10% Mg doping and a solid solution reaction at 25% Mg doping in the high voltage region. Moreover, the results of resonant inelastic X-ray scattering (RIXS), X-ray absorption spectroscopy (XAS), and density functional theory (DFT) calculations reveal that Mg doping with an appropriate concentration can increase the Ni redox activity, but at the same time it suppresses the O redox activity due to the reduced Ni content and the competing mechanism between Ni and Mg. However, it is found that the 'O bound to Mg' acts as an additional redox center, which is triggered at high voltages (>4.0 V). This O redox process occurs at a slightly higher redox potential than that occurring when O is only bound to Ni, resulting in the observed sloping potential profile for the Mg-doped material. Although different Mg doping concentrations can induce different shapes in the high voltage region of the potential profiles, they are found to have a greater effect on the average voltage than on the cycling stability. This new finding highlights the complex interplay between structure, redox chemistry, and doping in Na layered oxides and provides an additional explanation toward understanding doping effects in layered oxides.

2. Results and Discussion

A series of Mg-doped compounds, $NaMg_xNi_{0.5-x}Mn_{0.5}O_2$ ($x = 0$, 0.10, 0.15, 0.20, 0.25, denoted as O3-NaM_xNMO) were produced by a solid-state synthesis method. X-ray diffraction (XRD) patterns of these materials, evidencing pure O3 structures with a tiny amount of NiO impurity, and scanning electron microscopy (SEM) images of the µm-sized particles of O3-NaNMO and O3-$NaM_{0.10}$NMO are shown in Figures S2 and S3 (Supporting Information). The electrochemical properties of these samples were evaluated in coin cells (half-cell geometry with sodium metal as the counter electrode) over a voltage range of 2.5–4.4 V at a current density of 20 mA g^{-1}. As shown in **Figure 1a**, the first charge/discharge capacities of O3-NaNMO, O3-$NaM_{0.10}$NMO, O3-$NaM_{0.15}$NMO, O3-$NaM_{0.20}$NMO, and O3-$NaM_{0.25}$NMO are 217/194, 198/157, 202/127, 161/115, and 180/94 mAh g^{-1}, respectively. As the Mg content increases, the discharge capacities significantly decrease compared to the undoped material. The doped samples also exhibit a large amount of irreversible capacity, particularly in the case of O3-$NaM_{0.25}$NMO. This behavior is expected due to the substitution of electrochemically active Ni sites with electrochemically inactive Mg. Despite the reduced initial capacity, all Mg-doped materials demonstrate improved capacity retention compared to the undoped sample (see Figure S4, Supporting Information). This can occur due to different reasons, but one needs to keep in mind that lowering the electrode capacity typically leads to improved cycle life. This is simply because less charge per cycle is being transferred, which causes less stress ("shallow cycling"). The best stability is therefore found for O3-$NaM_{0.25}$NMO. Considering the best compromise between capacity and stability, 10% Mg doping is the most favorable concentration for O3-$NaNi_{0.5}Mn_{0.5}O_2$. The capacity retention of the O3-$NaM_{0.10}$NMO material is 49% after 200 cycles, which is a marked improvement over the almost complete capacity loss (≈100%) of O3-NaNMO without doping over the same number of cycles (see Figure 1d). However, it is noteworthy that the doped materials exhibit significant differences in their potential profiles, especially in the high voltage region above 4.0 V. Mg doping is found to suppress the high-voltage plateau while inducing a sloping profile when the charging voltage is increased to 4.4 V, and the sloping behavior is more pronounced as the Mg doping content increases. Similar behavior was also found for the doped P2-$Na_{0.67}Ni_{0.33}Mn_{0.67}O_2$ with the different Mg

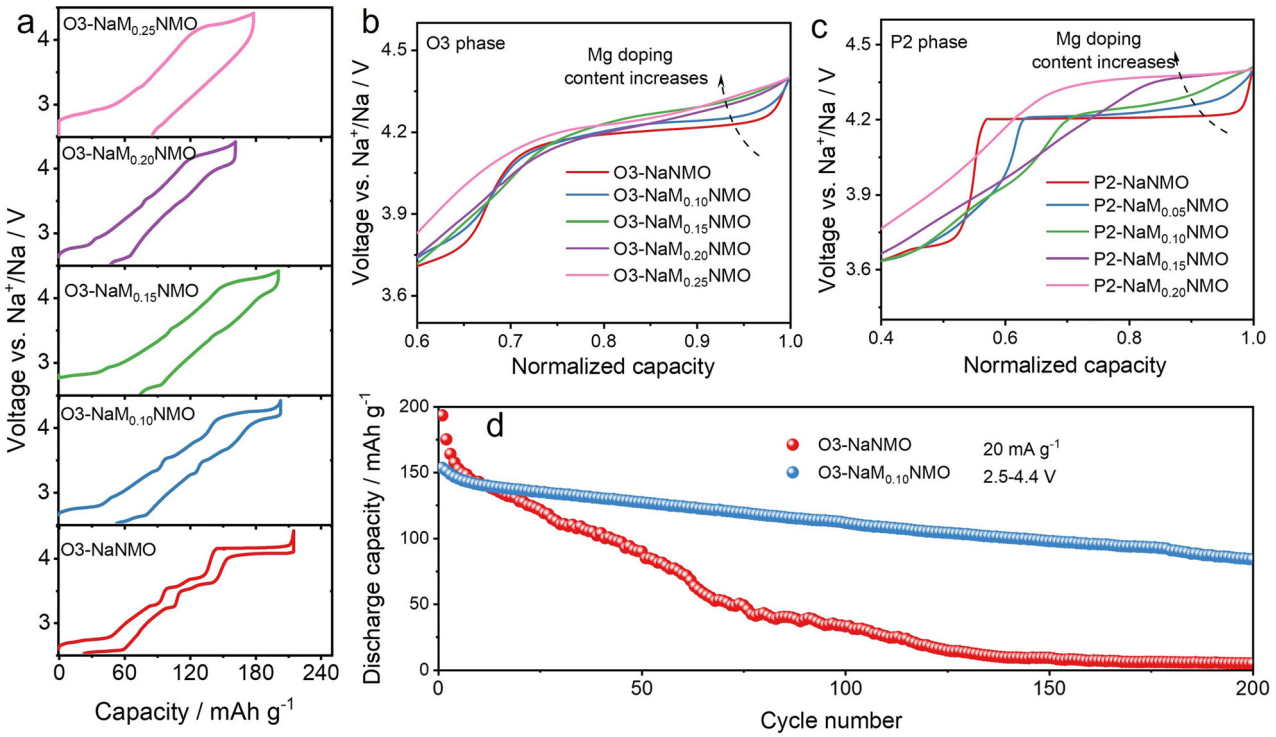

Figure 1. Electrochemical properties of the Mg doped O3-$NaNi_{0.5}Mn_{0.5}O_2$ at 20 mA g^{-1} in the voltage range of 2.5–4.4 V. a) The voltage profiles of O3-NaM_xNMO (x = 0, 0.10, 0.15, 0.20, 0.25) in the first cycle. b,c) The normalized voltage profiles of the Mg doped O3- and P2- type Ni-Mn based layered compounds, respectively. d) The long-term cycling performance of $NaM_{0.10}NMO$ at 20 mA g^{-1}.

concentrations (see Figure S5b, Supporting Information). These results suggest that Mg may play a similar role in both P2-NaNMO and O3-NaNMO.

To better understand the influence of Mg doping on the potential profiles, we normalized the charge capacity of each material by setting the maximum capacity to 1. This normalization was applied to O3-$NaNi_{0.5}Mn_{0.5}O_2$ and P2-$Na_{0.67}Ni_{0.33}Mn_{0.67}O_2$ with varying Mg doping levels. As observed in Figure 1b,c, the slope of the charge curves gradually increases with increasing Mg doping content in both Mg-doped systems. The only difference is that the P2 phases with 15% and 20% Mg doping show a new voltage plateau with a higher potential, but the Mg-doped O3 phases do not show such a plateau, which may be due to the phase differences between the two systems. The dQ/dV curves of the two Ni-Mn based layered compounds and P2-$Na_{0.67}Mg_{0.33}Mn_{0.67}O_2$ (P2-NaMgMnO) are shown in **Figures 2** and S6 (Supporting Information). For the Ni-Mn based layered compounds, it is clear that only Ni redox participates in the electrochemical process when the voltage is below 4.0 V. This is because the Mn in all the compounds has an oxidation state of +4 and is electrochemically inactive. With Mg doping, the oxidation peaks become weaker than those without doping, except for the peak located in the low voltage range (< 3.0 V) for the O3 phase (see Figure S6, Supporting Information). Deeper investigations of the low voltage range will be interesting to understand the doping effect on the O3 phase, but are beyond the scope of this article. Importantly, clear differences can be easily observed in the different intensities and locations of the oxidation peaks in the corresponding dQ/dV curves above 4.0 V.

As seen in Figure 2a, the P2-$Na_{0.67}Mg_{0.33}Mn_{0.67}O_2$, undoped O3-NaNMO, and P2-NaNMO show the sharpest and highest intensity peaks at different potential values over 4.0 V. The P2-NaMgMnO material shows the highest potential, followed by P2-NaNMO, and then O3-NaNMO. As the Mg doping content increases, the oxidation peak gradually shifts to higher potentials and becomes weaker for low doping concentrations. The oxidation peaks then split into two peaks when the doping content is over 15% for P2 and 20% for O3 phases. Although O3-$NaM_{0.25}NMO$ and P2-$NaM_{0.20}NMO$ show different intensities of the split oxidation peak, it is located at the same potential. These results show that Mg plays a similar role in influencing the potential profiles of O3-NaNMO and P2-NaNMO, indicating that the role of the dopant depends more on its content rather than on the structure type.

Interestingly, the split oxidation peak (see Figure 2a,b) at the lower potential closely resembles that observed in P2-NaNMO, indicating a similar redox process (Ni redox and 'O bound to Ni' redox) among the undoped and Mg doped materials. Meanwhile, the oxidation peak at the higher potential aligns with the characteristic location in P2-NaMgMnO. Notably, P2-$Na_{0.67}Mg_{0.33}Mn_{0.67}O_2$ is a well-established compound known to exhibit pronounced oxygen redox activity above 4.0 V, attributed to its distinctive Na–O–Mg configuration.[33] This suggests that Mg in Ni–Mn based layered oxides could similarly facilitate oxygen redox processes. The projected density of states (DOS) of the oxygen p-orbitals for the O3-$NaM_{0.10}NMO$ material at the fully charged state is shown in Figure 2d. It can be seen that the DOS exists over all simulated oxygen atoms ('All O') or sim-

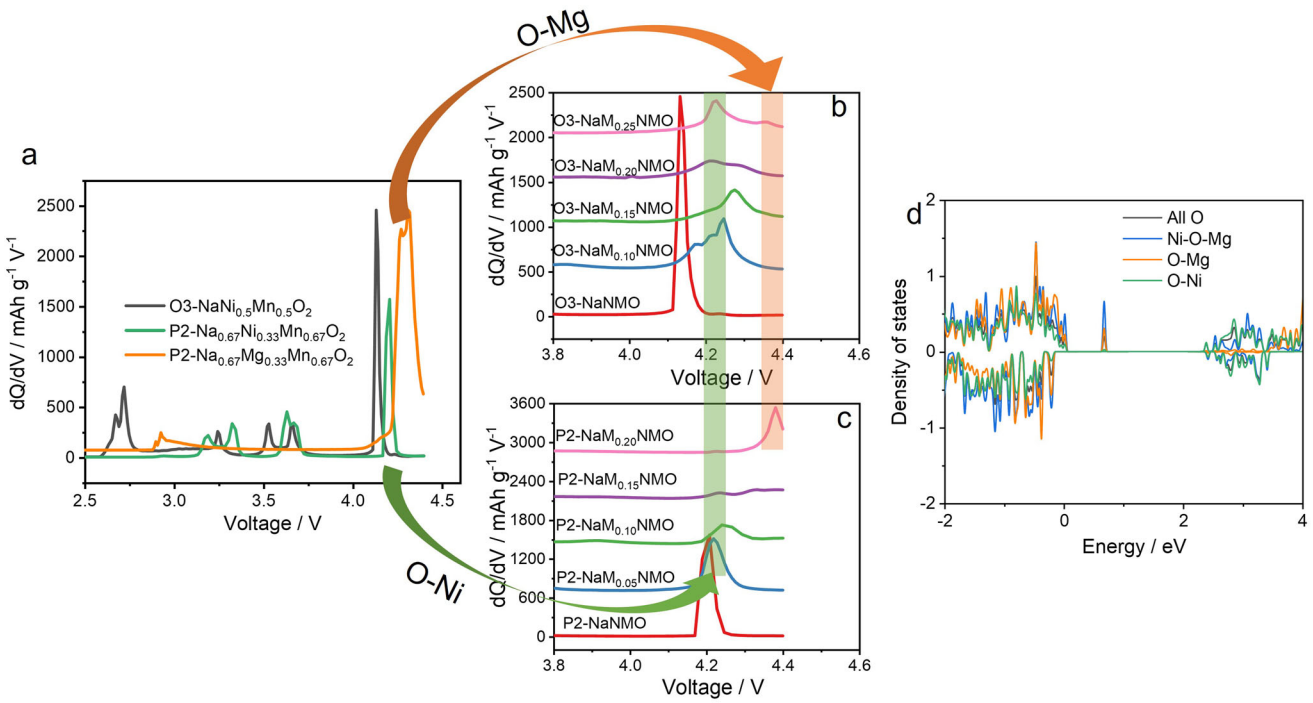

Figure 2. a) The dQ/dV curves of O3-$NaNi_{0.5}Mn_{0.5}O_2$, P2-$Na_{0.67}Ni_{0.33}Mn_{0.67}O_2$, and P2-$Na_{0.67}Mg_{0.33}Mn_{0.67}O_2$ during the first charge. b,c) The dQ/dV curves of O3-NaM_xNMO and P2-NaM_xNMO, respectively. d) Projected densities of states (DOS) of the oxygen p-orbitals for the fully charged O3-$NaM_{0.10}NMO$ material, normalized per oxide ion.

ulated oxygen atoms with specific binding environments (bound to at least 1 Ni and no Mg: 'O—Ni', bound to at least 1 Mg and no Ni: 'O—Mg', and bound to at least 1 Ni and at least 1 Mg: 'Ni—O—Mg'). All energies are normalized to the Fermi-Level. These results indicate that the first depleted state above the Femi-Level is almost exclusively caused by 'Ni—O—Mg' and 'O—Mg', hinting toward a distinct redox center for 'O bound to Mg'. Consequently, in the high-voltage region of Mg-doped Ni—Mn compounds, two distinct oxygen redox centers are present: one involving oxygen bound to Ni, and the other involving oxygen bound to Mg.

To elucidate how the new redox center influences the structural evolution of O3-$NaNi_{0.5}Mn_{0.5}O_2$, synchrotron-based *operando* XRD measurements were carried out for O3-NaNMO, O3-$NaM_{0.10}NMO$, and O3-$NaM_{0.25}NMO$, as shown in **Figures 3** and S8 (Supporting Information). The undoped material undergoes a complex series of phase transitions from O3 (rhombohedral) → O'3 (monoclinic) → P'3 (monoclinic) and P3 (hexagonal) → O'3 (monoclinic) → O3 (rhombohedral) during the first charge process; these phase transitions are reversible during the following discharge process.[18,20] Meanwhile, it is worth noting that the rhombohedral O3 phase at the fully charged state shows a decrease in the *c* lattice parameter of ≈17% compared to the parent O3 phase before charging, which is in line with previous studies by Komaba et al.[20]

With Mg doping, the phase behavior of the electrodes changes significantly during sodiation. In the low voltage region (below 3.0 V), in contrast to the complex phase transition (O3→O'3→P3) that occurs in the undoped material, the two Mg-doped materials show similar shifts in their reflections below 3.0 V, but without any phase transitions. O3-$NaM_{0.10}NMO$ shows a direct phase transition from O3 to P3 phase at ≈3.0 V (see Figure 3b), and O3-$NaM_{0.25}NMO$ shows a short-mixed phase region with O3, O'3, and P3 at ≈3.0 V (see Figure S8, Supporting Information and Figure 3c). Later, similar to the change of the undoped material at 3.7 V, the two doped materials both show a single P3 phase with a continuous shift of the main reflection to lower angles, indicating an expansion of the interlayer spacing upon charging. However, the two doped materials show completely different phase transitions above 3.7 V. For O3-$NaM_{0.10}NMO$, the main reflection located at 3.7° slightly shifts back to a larger angle due to formation of the O'3 phase at 4.1 V, as evidenced by the characteristic $100_{O'3}$ reflection located at 8.3° for O3-$NaM_{0.10}NMO$. When charged to 4.2 V, the main reflection weakens, and later a new reflection becomes visible at a higher angle, indicating the formation of a new phase at the fully charged state. This phase is called OP2, which is similar to the reported OP4 phase in the P2-$Na_{0.67}Mg_{0.10}Ni_{0.23}Mn_{0.67}O_2$.[34] While for O3-$NaM_{0.25}NMO$, there is no phase transition above 4.0 V until the fully charged state, and only a continuous shift of the main reflection to lower angles after the first phase transition from O3 to P3 at 3.0 V is found. This indicates a solid-solution reaction of a pure P3 phase in the high voltage region, and the corresponding *c* lattice parameter shows an expansion of ≈5.65%.

During discharge, the OP2 phase of O3-$NaM_{0.10}NMO$ shows a comparably high reversibility. The main reflection gradually shifts to a lower angle with the formation of the monoclinic O'3 phase at ≈4.0 V, as evidenced by the appearance of the characteristic $111_{O'3}$ reflection at 9.6°. Subsequently, similar to the observation of the O'3 during charging, the position of the main re-

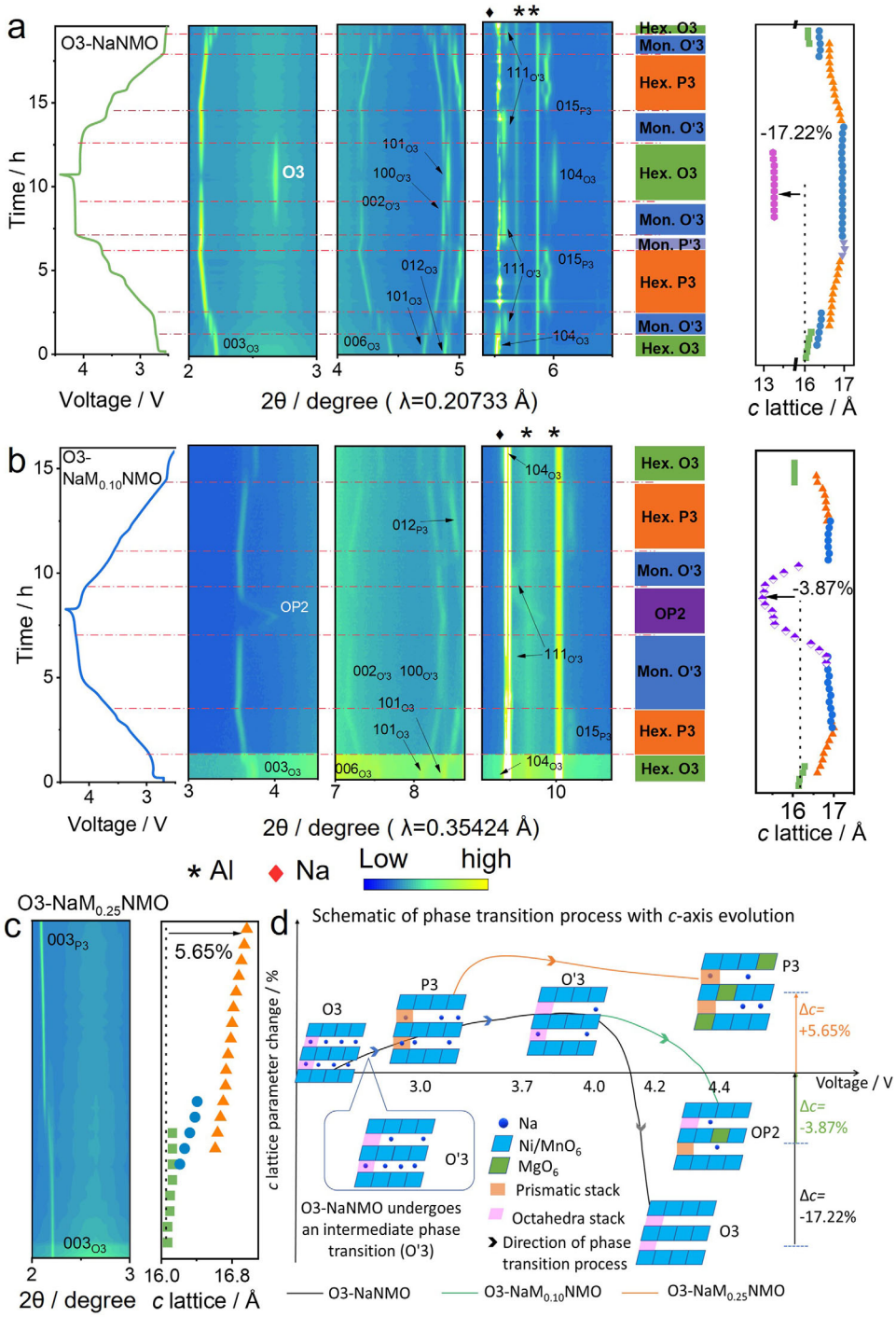

Figure 3. Contour plots of synchrotron-based *operando* X-ray diffraction, the corresponding phases and *c* lattice parameters for a) O3-NaNMO (λ = 0.20733 Å) and b) O3-$NaM_{0.10}$NMO (λ = 0.35424 Å). c) The contour plots of the main reflection (003) (λ = 0.20733 Å) and the corresponding *c* lattice parameter for O3-$NaM_{0.25}$NMO. d) Schematic diagram of the phase transition for the three materials during the first charge process.

flection remains stable until being discharged to 3.6 V. Upon further discharging, the $111_{O'3}$ reflection disappears and the main reflection gradually shifts to a higher angle, followed by the appearance of the 012_{P3} reflection at 8.5° and the 015_{P3} reflection at 10.15°, respectively, signifying a phase transition from O'3 to P3. When being discharged to 3.0 V, the O3-$NaM_{0.10}$NMO material undergoes a further phase transition from P3 back to the original O3 structure, similar to the undoped counterpart. This demonstrates a fully reversible phase transition pathway during cycling. In contrast, the formation of the OP2 phase results in only a ~3.87% decrease along the *c*-axis, suggesting that 10% Mg doping effectively suppresses structural changes. This structural

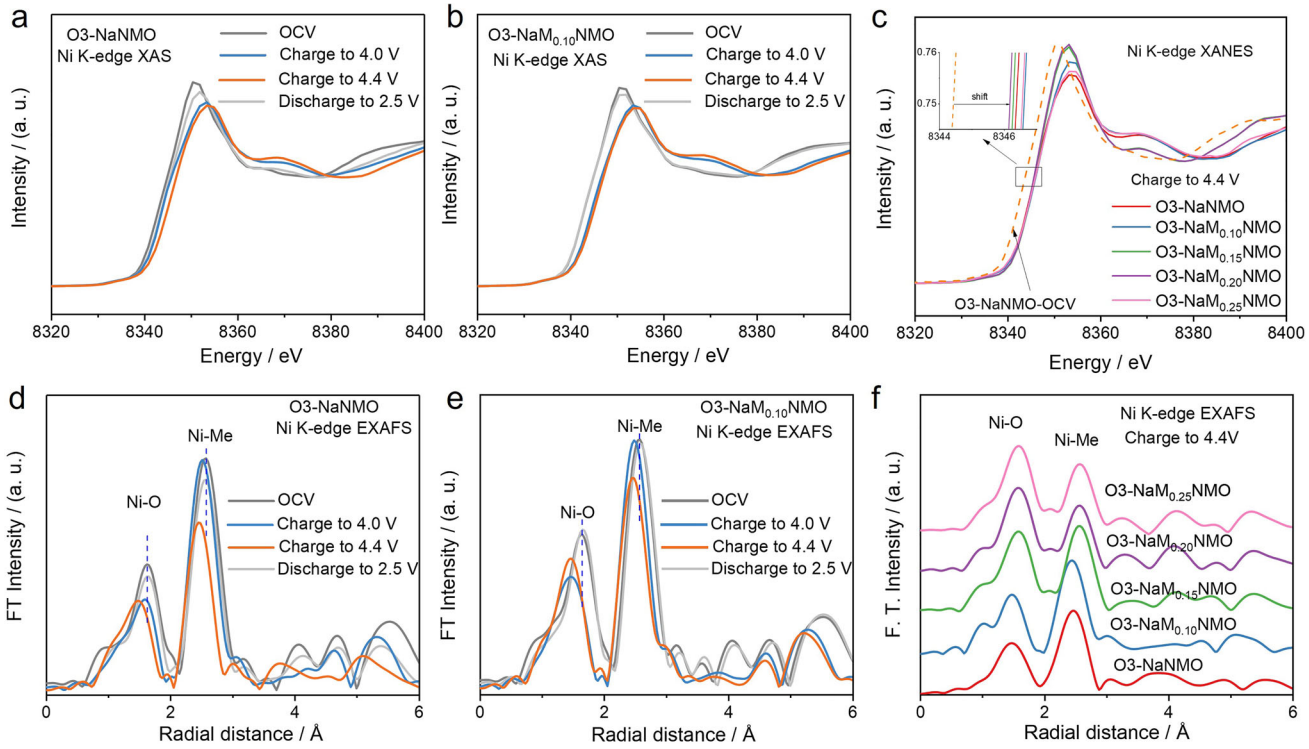

Figure 4. Ex situ Ni *K*-edge XANES data and the corresponding EXAFS data. a,d) O3-NaNMO and (b,e) O3-$NaM_{0.10}$NMOat different charge/discharge states. c,f) O3-NaM_xNMO (x = 0, 0.10, 0.15, 0.20, 0.25) at the charge to 4.4 V state. Insets in Figure c magnify the region between 8344–8347 eV to highlight the different energy shifts of O3-NaM_xNMO.

stabilization is further corroborated by the improved cycling stability observed in the Mg-doped material.

As observed by comparing the phase transition and the *c* lattice parameter change among these materials during the charge process (see Figure 3d), although Mg doping can suppress the formation of the intermediate phase (O'3) below 3.0 V, the transition from O phase to P phase is inevitable in this period. Upon charging to 4.0 V, the transition becomes less complicated as the Mg doping content increases. In the high voltage region, 10% Mg facilitates the formation of an intermediate OP2 phase, while 25% Mg completely suppresses the P-to-O phase transition by promoting a solid-solution type reaction. Both effects help mitigate changes in the lattice parameters. Compared to the O3-$NaM_{0.25}$NMO sample, the additional phase transitions from P3 to O'3 to OP2 for O3-$NaM_{0.10}$NMO are found to reduce the lattice expansion to ≈9.52% at the fully charged state, and the additional phase transitions from P3→O'3→O3 for O3-NaNMO result in a sudden ≈23% decrease at the same time. However, the O3-NaNMO material shows better structural reversibility than the O3-$NaM_{0.10}$NMO sample, followed by the O3-$NaM_{0.25}$NMO sample (according to the electrochemical performance in Figure 1a). Combined with the electrochemical properties, we can understand that the phase transitions are favorable for achieving high capacity in the electrode materials and maintaining structural reversibility, but they accelerate the aging process to some extent, especially in the high voltage range.

To identify changes in the valence states of Ni and Mn during charging and discharging, ex situ X-ray absorption near edge structure (XANES) analysis was performed at the Ni and Mn *K*-edges for O3-NaM_xNMO (x = 0, 0.10, 0.15, 0.20, 0.25) during the first cycle. **Figure** 4a,b show the Ni *K*-edge and Figure S10a,b (Supporting Information) show the Mn *K*-edge spectra for the undoped and the 10%-Mg doped samples at different states of charge, i.e. at OCV, charge to 4.0 V, charge to 4.4 V, and discharge to 2.5 V. Apparently, the Ni redox is involved in the electrochemical reaction throughout the charging process for all materials, as evidenced by the obvious shift in edge energies to higher values (see Figure 4a,b). While O3-NaNMO and O3-$NaM_{0.10}$NMO both show slight shifts of the edge energy between the charged states at 4.0 V (blue curve) and 4.4 V (orange curve), especially for the O3-$NaM_{0.10}$NMO material, demonstrating that the two materials show an overall lower amount of Ni redox above 4.0 V. However, the undoped and 10% Mg-doped materials both deliver a high charging capacity in this regime. Moreover, the Mn redox is electrochemically inactive due to its already stable valence (Mn^{4+}) among these two materials, see Figure S10 (Supporting Information). These results suggest that there is another redox process that contributes to the high capacity in the undoped and 10% Mg-doped materials above 4.0 V. The likely cause is oxygen redox, which has been found for many P-type Ni-Mn based layered oxides for SIBs.[35,36]

In addition, a comparison of the Ni *K*-edge XANES of the undoped and Mg–doped materials at the OCV and the charge to 4.4 V states is shown in Figure S9 (Supporting Information) and Figure 4c, respectively. As observed at the OCV state, the curves of the O3-NaNMO and O3-$NaM_{0.10}$NMO samples coincide perfectly

at the edge, implying that the Mg doping does not affect the Ni oxidation at the initial state. While at the fully charged state (4.4 V), the O3-NaM_xNMO (x = 0, 0.10, 0.15, 0.20, 0.25) materials show different energy shifts compared to the OCV state (see Figure 4c). The O3-$NaM_{0.10}NMO$ material shows overall the highest energy shift among these samples, followed by O3-$NaM_{0.25}NMO$, O3-NaNMO, O3-$NaM_{0.15}NMO$, and O3-$NaM_{0.20}NMO$. This implies that Mg doping with a suitable doping concentration can enhance the Ni redox activity, which is found to be greatest in the case of 10% doping content. When discharged to 2.5 V (see Figure 4a,b), the XANES spectrum for the O3-$NaM_{0.10}NMO$ sample is similar to that of the respective OCV states, while that of the undoped material differs. This indicates a better redox reversibility for the 10% Mg-doped compound.

The coordination environment of Ni and Mn at the various states of charge was evaluated by extended X-ray absorption fine structure (EXAFS) analysis for O3-NaM_xNMO (x = 0, 0.10, 0.15, 0.20, 0.25) (see Figure 4d–f), and Figures S9 and S10 (Supporting Information). The O3-NaNMO and O3-$NaM_{0.10}NMO$ materials undergo different changes when charging to the high voltage region (4.0 and 4.4 V), corresponding to their individual phase transitions above 4.0 V. The undoped material shows an obvious decrease in interatomic distance, and a slight decline in coordination number for both Ni—O and Ni—Me (where Me indicates Mn, Ni or Mg) shells. In comparison, the 10% Mg-doped material shows only an obvious increase in the coordination number of the Ni-O shell as the charging voltage increases to 4.4 V. The unchanged Ni—O bond length of O3-$NaM_{0.10}NMO$ fits well with the proposed solid solution-type reaction found from the *operando* XRD results in the high voltage region. As for the EXAFS at the Mn K-edge, the O3-NaNMO and O3-$NaM_{0.10}NMO$ materials show only significant changes at the Mn-Me shell at the charged states, which is induced by the change of Ni environment. These results indicate that all these materials have a relatively stable Mn environment. In the subsequent discharge state at 2.5 V, the curves of the undoped material and 10% Mg-doped material are not found to return to their original OCV state, which indicates that the coordination environment of Ni is only partially reversible for all samples, especially in the case of the undoped material. With more Mg doping in O3-$NaNi_{0.5}Mn_{0.5}O_2$, the radial distances of the Ni-O shell and the Ni-Me shell both increase slightly, indicating that the Mg doping can effectively suppress changes in the Ni environment, and the appropriate doping content can enhance the reversibility of the Ni redox activity.

O *K*-edge resonant inelastic X-ray scattering (RIXS) was measured to elucidate the impact of the Mg doping on the degree of oxygen redox. **Figure** 5a,b show the RIXS data for O3-NaNMO and O3-$NaM_{0.10}NMO$ at the OCV, charged to 4.4 V, and discharged to 2.5 V states. A unique peak located at an energy loss of 8 eV is related to the O—O signature, which is widely associated with an oxygen redox feature.[13,14,37,38] In Figure 5a,b, this signal is only visible after charging to 4.4 V, and could be observed in these two materials, indicating that oxygen redox does indeed occur at the fully charged state. However, the intensity of this signal is different between the two samples, with the highest intensity being observed for O3-NaNMO, followed by O3-$NaM_{0.10}NMO$. Meanwhile, the RIXS maps (Figure 5d,e) with excitation energy ranging from 526 to 534 eV were also conducted at the fully charged state (4.4 V). The fingerprint signal of the oxygen redox is highlighted with a light blue circle, which corresponds to the signal at an energy loss of 8 eV as discussed with the 1D RIXS spectra.[13,14,35–38] It can be observed that the intensities of this fingerprint signal are slightly different amongst the materials, but their intensities also follow the observations in the 1D RIXS spectra. Moreover, the progression of the peaks close to 0 eV has been magnified and is shown in Figure 4c. A series of peaks with gradually decreasing intensity can be observed for the two samples at a state of charge of 4.4 V, which are reported to reflect the vibration between O-O bonds.[13,14,38] The intensities of these peaks are associated with the strength of the oxygen redox signal at an energy loss of 8 eV. As expected, the undoped material exhibits peaks with higher intensity, while the 10% Mg-doped material appears to have relatively lower intensity. The distance between the first peak and 0 eV for the two samples is close to that reported for the vibration of molecular O_2 by Bruce et al.[13,14,38] Although the presence of molecular oxygen in the lattice of these materials is a matter of debate, the results nevertheless indicate that oxygen redox occurs in the two materials when being charged to 4.4 V, and that the Mg doping can reduce the activity of the oxygen redox. We are aware that there is an intense discussion on the nature of the oxidized oxygen species, especially considering the use of RIXS for the determination of trapped molecular oxygen.[39] Given the ongoing debate, we have chosen not to engage in a detailed discussion about the exact nature of the oxidized oxygen species in our work, even though we do observe evidence of oxygen redox in general. However, the data presented in our manuscript will be valuable to RIXS experts who are better positioned to further investigate and interpret the exact nature and content of these oxidized species.

RIXS spectra for the O3-NaM_xNMO (x = 0.15, 0.20, and 0.25) materials at the fully charged state were also collected and are shown in Figure 5f. Interestingly, we observe a continuously decreasing intensity of the oxygen redox signals among these samples, especially for the O3-$NaM_{0.25}NMO$ material, which shows a similar curve shape to the undoped materials and the 10% Mg-doped materials in the OCV/discharged states. These results indicate a decrease of the oxygen redox activity as the Mg doping content increases to 25%. This is consistent with our proposed competing mechanism that the degree of O-redox becomes smallest for a Mg/Ni ratio of 1, while the degree of O-redox increases for ratios greater than or less than 1. In the O3-$NaM_{0.10}NMO$ material, the Mg/Ni ratio is only 1/4, i.e. a strong O-redox can still be expected. When increasing the Mg content to 25%, the Mg/Ni ratio gradually increases to 1. Therefore, the O3-$NaMg_{0.25}Ni_{0.25}Mn_{0.5}O_2$ material shows the lowest oxygen redox signal (see Figure 5f). Overall, it is reasonable to believe that the competing mechanism between Ni—O and Mg—O also exists in the Mg-doped O3-$NaNi_{0.5}Mn_{0.5}O_2$, accordingly leading to a change of the oxygen redox. To compare the contributions of the Ni and O redox for the first charge capacities of all materials, we conducted normalizations of the Ni and O redox based on the energy shift at the Ni K-edge XANES (Figure 4c) and the intensity ratio of A/B at the O K-edge RIXS (Figure 5f), respectively (please find details in the supporting information in Figure S11 and Tables S1 and S2, Supporting Information). Although O3-$NaM_{0.10}NMO$ shows the highest activity of the Ni redox, the differences among these materials are relatively small compared to the O redox. This is due to the fact that the oxygen redox occurs

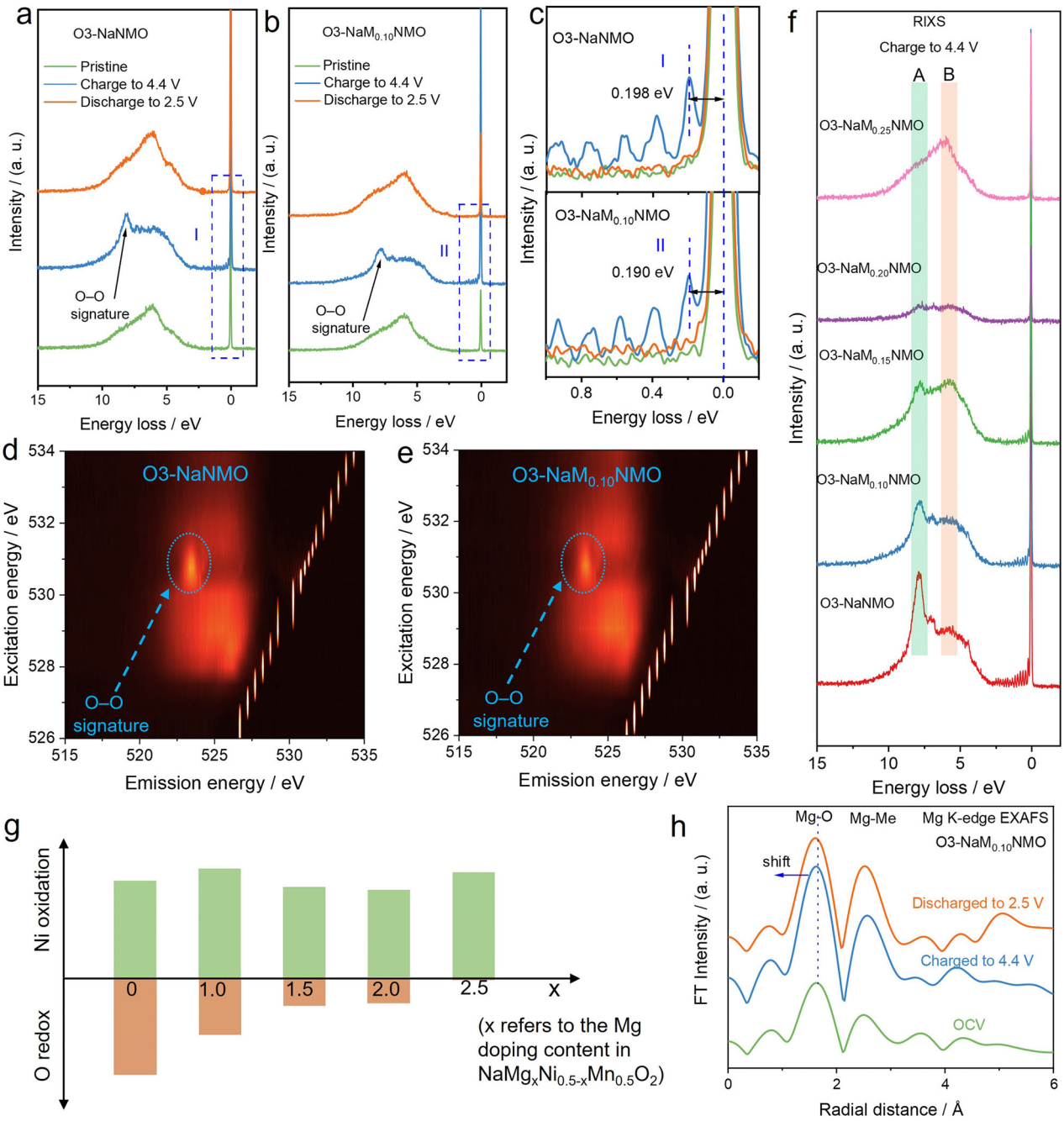

Figure 5. O *K*-edge RIXS spectra with an excitation energy of 531 eV for a) O3-NaNMO and b) O3-$NaM_{0.10}$NMO at OCV, charged to 4.4 V, and discharge to 2.5 V states. c) Magnified RIXS spectra for the two samples in the three states. O *K*-edge RIXS maps with excitation energy ranging from 526 to 534 eV for d) O3-NaNMO and e) O3-$NaM_{0.10}$NMO. f) A comparison of RIXS spectra for O3-NaM_xNMO (x = 0, 0.10, 0.15, 0.20, 0.25) at the charge to 4.4 V state. g) A summary of the O redox contribution and Ni oxidation of NaM_xNMO. The height of the green bars represents the maximum oxidation state of each material at the fully charged state, and the height of the orange bars represents the amount of O redox contribution, respectively. h) Mg K-edge EXAFS at OCV, charge to 4.4 V, and discharge to 2.5 V states.

only in the high voltage region. When we compare the difference of the O redox among each other, the 10% Mg doping causes the most dramatic change, indicating that trace doping significantly affects the O redox.

Although a strong oxygen redox was found to exist in O3-NaM_xNMO (x< 0.25) at 4.4 V, the triggering mechanism of this O redox remains unclear, especially for the Mg-doped materials. In order to demonstrate the difference of the oxygen redox between the undoped and the Mg-doped materials, ex situ Mg *K*-edge EXAFS was performed for O3-$NaM_{0.10}$NMO and is shown in Figure 5h. A shortening of the Mg—O distance can be observed after charging to 4.4 V. However, as the valence of Mg re-

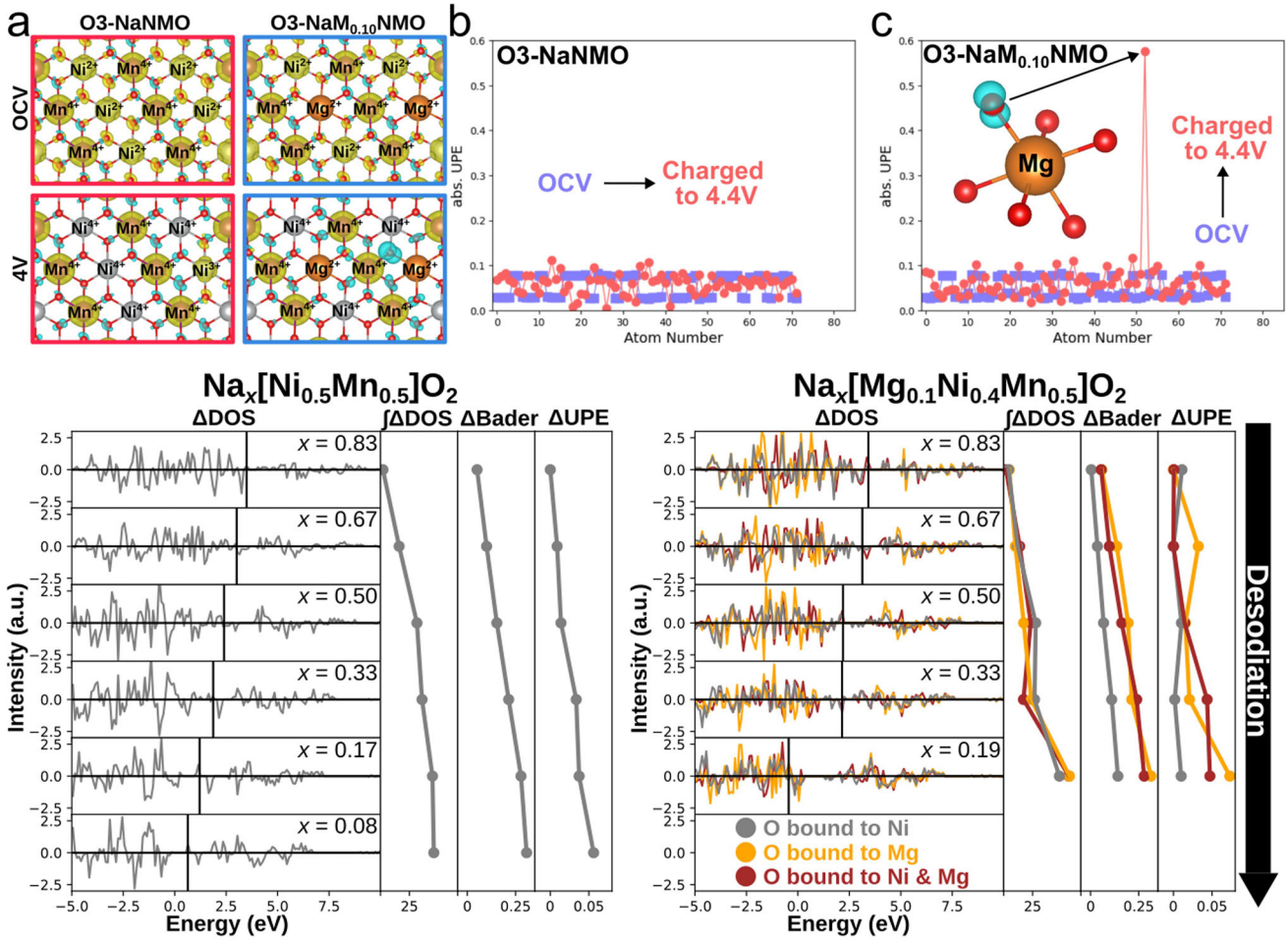

Figure 6. a) The calculated spin density differences (SDD), with a yellow color for spin-up and a blue color for spin-down at an iso-value of 0.02 UPE/Å^3 for the different materials in the 4.4 V (charged state) and OCV state (discharged state), along with assigned charges. The absolute number of unpaired electrons (UPE) on the oxygen (O) ions of b) O3-NaNMO and c) O3-Na$M_{0.10}$NMO as obtained from HSE06-DFT calculations. The plots visualize oxygen redox and indicate one strong oxygen oxidation in the Mg-doped material of an 'O bound to Mg'. d) Projected densities of states (DOS) of oxygen p-orbitals relative to their DOS of the previous (higher) sodium concentration for O3-NaNMO (left) and O3-Na$M_{0.10}$NMO (right) at different sodium concentrations (top to bottom).

mains the same, this change should be caused by the neighbouring O, indicating a more pronounced electrochemical activity of 'O bound to Mg'. During subsequent discharging to 2.5 V, there is no change in the Mg-O distance from that of the charged to 4.4 V state, indicating that the shift in the Mg-O distance is irreversible. This is consistent with the lower degree of structural reversibility of O3-Na$M_{0.10}$NMO. Combining the results from RIXS measurements and Mg *K*-edge EXAFS, one can conclude that the oxygen redox in the Mg-doped materials can be attributed to two trigger centers, Ni and Mg, which may cause different electrochemical behaviors in the high voltage region.

To further elucidate the redox processes in the undoped and the 10% Mg-doped materials, we performed density functional theory (DFT) calculations. From the aforementioned discussion, it is clear that the redox behavior of these two materials is dominated by Ni redox from Ni^{2+} toward Ni^{4+} (see **Figure 6a**; Figure S12a,b, Supporting Information as well as corresponding analysis in Supporting Information for further details). As for the oxygen, the two compositions show quite some fluctuations slightly above 0 UPE (number of unpaired electrons) at the OCV and fully charged state (Figure 6b,c). Most of UPE on oxygens show a similar, minor drift toward 0.1 UPE for the OCV state. These deviations can be interpreted as delocalization of the charges on the transition metals, especially nickel, as the calculated UPE of ca. 1.7 is lower than the theoretical value of 2 for Ni^{2+} ($t_{2g}{}^6e_g{}^2$ cf. Figure S12a,b, Supporting Information). This delocalization is also visible in the spin density difference (SDD) plots of the discharged materials in Figure 6a, as mainly oxygen anions bound to nickel ions show some additional spin-up density. When being charged to 4.4 V, the fluctuations in UPE values on oxygen must be assigned not only to delocalization of the transition metal oxidation but also to direct oxidation of the oxygen ions, which agrees with the experimental RIXS measurements (Figure 5). In particular, one oxygen ion (out of 72) in the O3-Na$M_{0.10}$NMO material shows a very strong oxidation with more than 0.5 UPE (cf. Figure 6c). This strong oxidation can formally be assigned to an

oxidation of O^{2-} to O^{1-} that would have a theoretical change of UPE from 0 to 1 ($2s^22p^6 \rightarrow 2s^22p^5$). However, such a strong localization of the oxidized oxygen is probably not realistic, and the anionic redox is most likely more delocalized over various oxygen anions in the same binding environment. The over-localization might be an artifact of the employed hybrid functional, but a similar result is also obtained when considering different magnetic orderings (results shown in Figure 5b,c, ferro-magnetic and antiferromagnetic ordering was tested as well) and supercell sizes (a cell half as large in the a-dimension was tested as well). Nevertheless, it should be noted that this oxygen ion is directly bound to a Mg^{2+} ion which supports the experimental hypothesis that oxygens bound to Mg ions are oxidized more strongly. It can be assumed that a driving force for the oxidation of oxygens bound to Mg is the electrostatic interaction, as it should have the smallest decrease of attractive forces for decreasing the negative charge of an oxygen next to the cation with the smallest positive charge (Mg^{2+}).

To further verify that 'O bound to Mg' is indeed a distinct redox centre, further DFT calculations at various different sodium concentrations were performed and the electronic structures of oxygens were analysed. The results are summarized in Figure 6d. The Fermi levels are indicated by vertical lines. Differences between spin-up and spin-down channels are added in the plots such that simple shifts between the channels cancel out. The total DOS of oxygen p-orbitals are given in Figure S13 (Supporting Information). Next to the DOS, the integral of depleted states above the Fermi level relative to the fully sodiated materials is shown. Changes in Bader charges and unpaired electrons (UPE) relative to the fully sodiated materials are given as well. In the right plot oxygen signals are divided into 3 groups: 'O bound to Ni' (and not Mg), 'O bound to Mg' (and not Ni), and 'O bound to Ni & Mg'. In the left plots for O3-NaNMO all oxygen atoms are bound to at least one Ni resulting in only one group: 'O bound to Ni'.

Analysis of the electronic structures of oxygen atoms reveals that 'O bound to Mg' is a new redox center that is only present in the Mg-doped material. Consistently through all employed analysis methods (integration of depleted DOS states, Bader charges, and UPE), oxygen atoms that are bound to Mg behave differently from other oxygen atoms, e.g., oxygen atoms that are just bound to Ni and Mn. More precisely, 'O bound to Mg' shows a stronger redox activity in the calculated electronic structures as the yellow and red curves ('O bound to Mg' and 'O bound to Ni & Mg') in the right part of Figure 6d are always above the grey one ('O bound to Ni'). The larger integral of depleted states, higher increase of Bader charge (more positive charge), and larger increase of UPE (more toward $2s^22p^5$, O^{1-}) in 'O bound to Mg' clearly indicates a stronger anionic redox for these oxygen species. The separation of 'O bound to Mg' to the other oxygen atoms throughout all the different analysis methods gives strong evidence that 'O bound to Mg' is indeed a distinct redox center with different properties from the oxygen redox that can be found in the Mg-free O3-NaNMO material.

Even though the most oxidized single oxygen ions are found in the O3-$NaM_{0.10}$NMO material ('O bound to Mg'), the average change of Bader charges of oxygen atoms as well as the absolute value of the average Bader charges (Figure S14, Supporting Information) indicate a stronger oxygen redox in the Mg-free material, O3-NaNMO. However, the charge assignment made from the UPE in Table S3 (Supporting Information) shows a different tendency with less redox active oxygen and more redox active Ni. The difference might be explained by the fact that strong localization was assumed for assignment while smaller fluctuations in UPE were neglected. This highlights the difficulties of assigning precise charge states from electronic structures as results are dependent on the integration approach. Considering the experimental RIXS results (Figure 5) that indicate overall stronger oxygen redox in O3-NaNMO than in $NaM_{0.10}$NMO, it appears that the small fluctuations in UPE are indeed important for the studied materials and that the stronger oxygen redox observed in Bader charge analysis is in better agreement to experiment. Regarding the assignment from UPE it should be also mentioned that besides the too strong localizations of electrons, distorted coordination environments (similar to the different orbital splitting in Jahn-Teller distortion) can also cause fluctuations in UPE that result in a too low assigned oxygen redox. Manganese-Oxygen and Oxygen-Oxygen pair distribution functions (PDFs) over machine learned force field (MLFF) ab initio molecular dynamics (AIMD) runs reveal some peak broadening that indicates the presence of local distortions (cf. Figure S12e,f, Supporting Information). However, the slightly stronger intensities of the first peaks in the Oxygen-Oxygen PDFs for O3-NaNMO than for O3-$NaM_{0.10}$NMO also give a hint for stronger oxygen redox in the simulations of O3-NaNMO (lower negative charge on oxygen atoms → less electrostatic repulsion → shorter O-O distances). However, for both materials, the Oxygen-Oxygen PDFs (Figure S12f, Supporting Information) show no contributions in the bounding region of oxygen (anions), thus no indication of (irreversible) oxygen dimerization was found in the simulation studies. However, as the rather short simulation times of 20 ps might hinder oxygen dimers to form, the oxygen-vacancy formation-energies in the fully charged materials were calculated using DFT as well for the distinct binding environments discussed in Figure 6. The corresponding formation energies were: 2.17 eV for 'O bound to Ni' in O3-NaNMO, and 2.04 eV for 'O bound to Ni', 1.70 eV for 'O bound to Ni & Mg', and 1.82 eV for 'O bound to Mg' in O3-$NaM_{0.10}$NMO. Those energies are in a similar order of magnitude as values reported for other energy materials.[40,41] This confirms again that 'O bound to Mg' in O3-$NaM_{0.10}$NMO are the main anionic redox and oxygen vacancy-formation centres.

Overall, the DFT calculations support the finding that the capacity of the studied materials is dominated by Ni redox followed by oxygen redox. Regarding the oxygen redox behavior, the most important finding of the calculations is that the 'O bound to Mg' is a distinct redox center in O3-$NaM_{0.10}$NMO that is substantially different from other oxygen species in the structure. More precisely, stronger anionic redox is observed for 'O bound to Mg' in the simulations. While for the overall oxygen redox activity in O3-NaNMO and O3-$NaM_{0.10}$NMO, the computational results are less straight forward to analyse, it still seems that the overall average oxygen redox is stronger in O3-NaNMO. However, for both compositions no oxygen dimerization was observed in MLFF-AIMD simulations. The findings regarding the various oxygen redox activities agree well with the conclusions made from the experiments, thus supporting the proposed redox mechanisms and the distinct redox activity of 'O bound to Mg'.

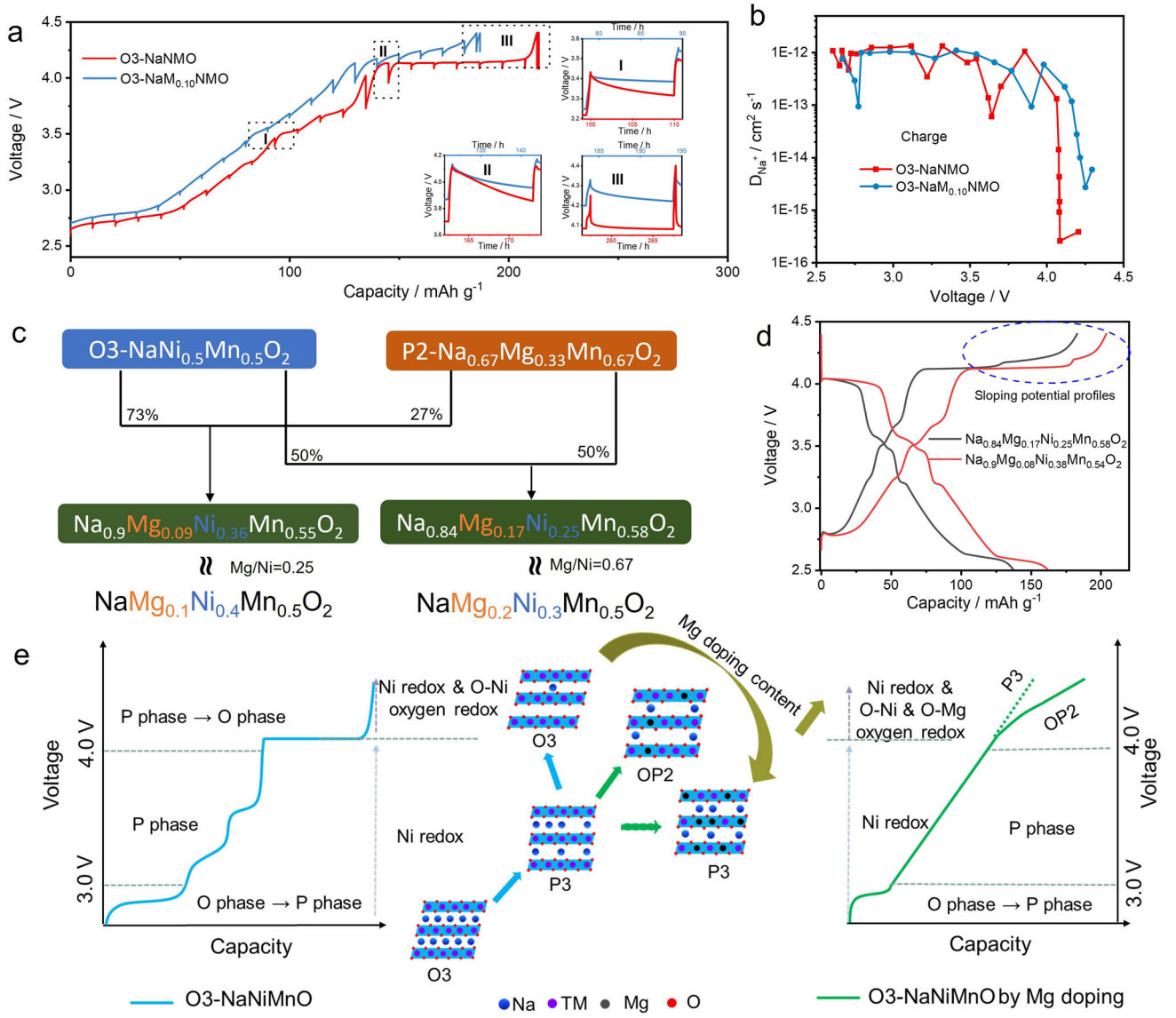

Figure 7. a) GITT analysis of O3-NaNMO and O3-NaM$_{0.10}$NMO during the 1st charging. The tests were performed with a 0.5 h pulse at C/10 followed by 10 h relaxation every step. Representative relaxation processes at the different charge states are shown in the insets. b) The corresponding calculated Na^+ diffusion coefficients of the two materials. c) A schematic illustration of the mechanically mixed materials between O3-$NaNi_{0.5}Mn_{0.5}O_2$ and P2-$Na_{0.67}Mg_{0.33}Mn_{0.67}O_2$ with the different ratios, d) the corresponding first charge/discharge curves of the two mixed materials. e) A summary of the Mg doping effect on the potential profile, phase transition, and redox activities.

3. Discussion

The relaxation behavior of the electrodes was studied for the compositions O3-NaNMO and O3-NaM$_{0.10}$NMO by using the galvanostatic intermittent titration technique (GITT), see **Figures** 7a and S17 (Supporting Information). The potentials of both materials after relaxation are still different, which supports that a thermodynamic effect causes the shift in potential. In general, TM redox below 4.0 V is known to have faster kinetics than oxygen redox above 4.0 V, which is in line with the higher Na diffusion coefficients for both materials below 4.0 V (see Figure 7b). Therefore, the two materials exhibit lower voltage drops below 4.0 V compared to above 4.0 V. Specifically, the insets highlight the voltage drops at 3.5 V (I), 4.0 V (II), and 4.4 V (III), respectively. The data also shows that the potential values for the Mg-doped sample in the sloping region remain above the ones for the undoped material. This suggests that there is indeed a shift toward higher potentials due to thermodynamic reasons, i.e. a shift caused by O bound to Mg.

The experimental and theoretical results both demonstrate electrochemical activity of Ni and O redox during the charging process for the undoped and the 10% Mg-doped materials. The prominent difference between these two materials is that the 'O bound to Mg' acts as an additional active redox center, which was demonstrated by Mg *K*-edge EXAFS, GITT, and DFT. This additional redox center has a slightly higher redox poten-

tial than that of the 'O bound to Ni', as evidenced by a higher potential of the dQ/dV peaks above 4.0 V in O3-$NaM_{0.25}$NMO and P2-$NaMg_{0.20}$NMO compared to the undoped O3-NaNMO and P2-NaNMO (see Figure 2b,c), which results in the unique sloping potential profile in the Mg-doped material. To further prove our hypothesis, a complementary experiment was performed by mechanically mixing O3-$NaNi_{0.5}Mn_{0.5}O_2$ (only Ni as the oxygen redox center) and P2-$Na_{0.67}Mg_{0.33}Mn_{0.67}O_2$ (only Mg as the oxygen redox center) with different ratios (7.3:2.7 and 1:1) to form new electrode materials, $Na_{0.9}Mg_{0.09}Ni_{0.36}Mn_{0.55}O_2$ and $Na_{0.84}Mg_{0.17}Ni_{0.25}Mn_{0.58}O_2$ (see Figure 7c). Among these two materials, the Mg/Ni ratios are 0.25 and 0.67, which are very close to the Mg/Ni ratios in O3-$NaMg_{0.10}Ni_{0.4}Mn_{0.5}O_2$ and O3-$NaMg_{0.20}Ni_{0.5}Mn_{0.5}O_2$, respectively. Apparently, these two materials both exhibit a similar sloping potential profile as observed in Figure 1a in the high voltage region (see Figure 7d). Moreover, it is due to phase segregation that two mixed electrode materials ($Na_{0.9}Mg_{0.09}Ni_{0.36}Mn_{0.55}O_2$, $Na_{0.84}Mg_{0.17}Ni_{0.25}Mn_{0.58}O_2$) show a flat high voltage plateau before the sloping potential profile, but it is invisible in the Mg doped O3-NaNMO materials. Therefore, we believe that the Mg has actually been doped into the crystal structure of $NaNi_{0.5}Mn_{0.5}O_2$, and the additional O bound to Mg as a redox center leads to the sloping potential profiles.

In the subsequent discharge process, however, the Mg-doped material shows a high voltage plateau quite similar to the undoped material, but with a smaller capacity contribution as the Mg doping content increases (see Figure 1a). This indicates similar redox processes, although they are not active to the same degree in all materials. The 'O bound to Mg' redox, however, appears to be largely irreversible. Therefore, the Mg-doped sample shows a high voltage plateau rather than a sloping profile on discharge. In the following cycles, the undoped material also shows sloping potential profiles (see Figure S4a, Supporting Information), we believe that structural degradation and polarization should be responsible for the shape change of the potential profiles during long-term cycling. Although the sloping potential contributes less to the cycling stability, it nevertheless has a greater effect on the average potential compared to potential profiles with plateaus in this region.

These results demonstrate that the sloping potential profile is caused by a variety of redox processes with different energies. In addition, many other dopants such as Li^+, Zn^{2+}, Cu^{2+}, Fe^{3+}, Ti^{4+}, etc. can also induce sloping potential profiles in Ni and Mn-based layered oxides above 4.0 V.[21,23,28,42,43] The dopants Li^+, Zn^{2+}, and Cu^{2+} have been shown to demonstrate similar properties to those of Mg in relation to how they trigger oxygen redox in P-type and Ni-free Mn-based layered oxides for SIBs.[13,44,45] It is therefore understandable that the sloping behavior is also related to the appearance of a new redox center, i.e. 'O bound to Li/Zn/Cu'. Although there are a few reports that Fe or Ti can trigger oxygen redox, the Fe^{3+}/Fe^{4+} redox couple has been shown to exist in many layered oxides above 4.0 V,[46] and Ti has been found to facilitate the oxidation of oxygen in layered oxides.[16] These reports collectively indicate that the appearance of a sloping (remaining) high voltage plateau in the potential profiles are related to the presence (absence) of additional redox centers in Ni-Mn based layered oxides.

4. Conclusion

In summary, Mg with different doping concentrations has been introduced into O3-$NaNi_{0.5}Mn_{0.5}O_2$ using a solid-state and high-temperature calcination method. The effects of Mg doping on the potential profiles, phase transitions, and redox activities are summarized in Figure 7e. Notably, Mg doping significantly enhances the cycling stability in a voltage range of 2.5—4.4 V compared to the undoped material, especially for the 10% doping concentration. Mg doping was found to suppress the formation of the intermediate phase (O'3) below 3.0 V, promoting a reversible OP2 phase at 10% doping and a solid-solution reaction into a single P3 phase at 25% doping in the high-voltage region (>4.0 V). Additionally, the sloping potential profile during charging was observed in the doped materials, which becomes more sloping as the Mg doping content increases. A combination of RIXS, XAS, and DFT calculations was used to demonstrate a strong oxygen redox in O3-$NaMg_xNi_{0.5-x}Mn_{0.5}O_2$ (x<0.25), and also revealed that the observed sloping behavior is related to the presence of an additional redox center associated with the 'O bound to Mg'. While this redox center is irreversible, the overall sloping behavior of the voltage profile is maintained over cycling. When comparing the effect of Mg doping in O3-$NaNi_{0.5}Mn_{0.5}O_2$, we find that the most characteristic differences are found in the first cycle, while over cycling, the properties become more and more similar, i.e. the type of dopant becomes less relevant. Future studies should therefore also be directed toward stabilizing the identified additional redox center over many cycles as only this way a higher average cell voltage of the battery could be achieved. The presence of additional redox centers is identified as the origin of a similar, previously reported, sloping electrochemical behavior found in Ni and Mn-based layered oxides with Li, Zn, Cu, Fe, and Ti doping. Overall, the findings provide a new route for understanding the effects of cation doping on the potential profile of layered oxides.

5. Experimental Section

Synthesis Methods: The P2-type materials were synthesized using a sol-gel method, following a procedure similar to that described in our previous report.[32] All O3-type materials were prepared via a solid-state method, as detailed below. Na_2O_2•Na_2O (100%, Alfa Aesar), Mn_2O_3 (>98%, Alfa Aesar), NiO (>99%, Alfa Aesar), MgO (>99.95%, Alfa Aesar), were used as the raw materials. An excess of 5mol% Na_2O_2•Na_2O was added to compensate for Na loss during the high temperature reaction, and 0.03 mol of product was synthesized in each experiment. All raw materials were mixed for 5 h using a planetary ball mill, then the mixture was fabricated as a pellet by pressing under 15 MPa pressure. After that, the pellet was calcined at 950 °C for 15h under O_2 atmosphere to obtain the final products. Before cooling down to 200 °C, the pellet was transferred to an Ar-filled Glovebox for further processing and measurement.

Electrochemical Characterization: The process of fabricating working electrodes is the same as previously reported.[32] The active material, Super P (SP, MTI Corp.), and polyvinylidene difluoride (PVDF, MTI Corp) were used in a weight ratio of 80:10:10 to form the electrodes. The PVDF binder was dissolved in N-methyl-2-pyrrolidone (NMP, Sigma Aldrich) with a concentration of 0.04 g mL^{-1}. The active material and Super P were mixed in a mortar for 10 min. The PVDF solution was then added, and mixed for another 5 min to form a homogenous slurry, which was then cast onto carbon-coated Al foil (MTI Corp.) with a doctor blade at a thickness of 300 µm. All the above-mentioned steps were carried out in an Ar-filled glove box (with H_2O and O_2 concentrations <0.1 ppm). The electrodes

were dried on a hot plate and then punched into 12 mm diameter electrodes, which were then dried in a Büchi at 120 °C for 12 h. 1 M $NaClO_4$ dissolved in PC:FEC (propylene carbonate, fluoroethylene carbonate, Sigma Aldrich) with a volume ratio of 98:2 was used as the electrolyte, and glass fiber (Whatman) as the separator. CR2032-type coin cells were assembled in an Ar-filled glove box with sodium metal (BASF Corp.) as the counter electrode. All cells were tested in a voltage range between 2.5 and 4.4 V (vs. Na^+/Na) using a constant-current protocol at various current densities with a Neware battery test system (Neware, CT-4008-5V10mA-164). For GITT measurements, at each step, the cells were charged/discharged at a current rate of 0.1 C for 30 min, then rested for 10 h.

Structural Characterization: Powder XRD was performed with a Bruker D2 Phaser XRD using Cu Kα radiation (λ = 1.5406 Å, 30 kV, 10 mA) between 10° and 60° (2θ) with a step of 0.02°/min. An air-tight low-background Si sample holder was used for all measurements. The *operando* XRD measurements for O3-NaNMO and O3-$NaM_{0.25}$NMO were carried out at beamline P02.1 at PETRA III at DESY (Deutsches Elektronensynchrotron) in Hamburg, Germany, using synchrotron radiation with an energy of ~60 keV (λ = 0.20733 Å).[47,48] The *operando* cells were designed in-house and assembled in an Ar-filled glovebox (H_2O and O_2 concentrations <5 ppm, provided by the beamline).[49] The electrochemical data were collected using a Biologic VMP-3 potentiostat with EC-Lab software, version 11.34. All the cells were allowed to rest for 20 min, then charged/discharged at 0.1 C over a voltage range of 2.5–4.4 V. The *operando* XRD data were collected sequentially as an ensemble of up to 5 cells operating simultaneously in Debye Scherrer geometry and with an acquisition time of 1 min per cell before moving to the next cell using a motorized X-Y stage with a travel range of 350 mm for both directions. The movement of the stages and triggering of the acquisition were controlled with a python3 script. Therefore, for each *operando* cell, a 1-min measurement was performed approximately every 6 min. Operando XRD measurement of O3-$NaM_{0.10}$NMO was performed at the DanMAX beamline, MAX IV Laboratory, Lund, Sweden, using home-designed pouch cells. The pouch cells were assembled at Ångström Laboratory, Uppsala University, and subsequently transferred to the beamline, where they were mounted in a specialized capable of accommodating up to six pouch cells simultaneously.[50] A Dectris Pilatus3 2 M CdTe detector was used to collect data in transmission mode with data collected every 2 min for each pouch cell. The wavelength was determined to be λ = 0.35424 Å from measurements of a LaB_6 standard. All Rietveld refinements of the XRD patterns were performed using GSAS I.

Resonant Inelastic X-Ray Scattering (RIXS): RIXS measurements were carried out at room temperature and under 10^{-8} mbar at the U41-PEAXIS end-station at BESSY II in Berlin, Germany.[51] The spectrometer was positioned at specular conditions relative to a 60 degree scattering angle and was optimized to a combined resolution of 90 meV using carbon tape. The excitation energy of each 1D curve was set to the O *K*-edge at 531 eV, and the acquisition time was 20 min. The excitation energy of each mapping around the O *K*-edge was 526 - 534 eV, and the acquisition time was 9 h. The coin cells used for the RIXS measurements were charged/discharged to the target voltage, then disassembled. The electrodes were washed with dimethyl carbonate (DMC), dried, and mounted onto double-sided Cu tape in an N_2-filled glovebox, then a transfer suitcase was used to transfer the samples to the measurement chamber.[32] The entire process was conducted under a N_2 atmosphere, without any exposure to air. Data were processed using the beamline software, Adler-4.0.

Spectroscopic Characterization: Ex situ Ni and Mn *K*-edge XAS were collected at room temperature at the KMC-2 end-station at BESSY II in Berlin, Germany in both transmission and fluorescence modes.[52] Reference spectra for energy calibration were collected before and after each sample measurement. XAS spectra were obtained by subtracting the pre-edge background from the overall absorption and normalizing with a spline fit using Athena software. The k^2-weighted EXAFS was Fourier transformed over a limited range of k from 3 to 11 $Å^{-1}$. Ex situ Mg *K*-edge XAS were collected in partial fluorescence yield (PFY) detection mode at room temperature in a UHV chamber at the PIRX beamline[53] at National Synchrotron Radiation Center Solaris[54] in Krakow, Poland. The data was processed using Athena software. The k^2-weighted EXAFS was Fourier transformed over a limited range of k from 3 to 8 $Å^{-1}$.

Scanning Electron Microscopy (SEM): SEM images were taken with a Phenom Pharos Desktop SEM from Phenom world using an accelerating voltage of 10 kV and a secondary electron detector.

DFT Calculations: To study the oxygen redox in the compounds from a first principles' perspective, we also performed density functional theory (DFT) calculations. Spin-polarized calculations within the projector augmented wave (PAW) method[55] as implemented in the *Vienna ab into simulation package* (VASP)[56] were conducted. Models were created as 4 × 3 × 1 supercells in the O3 phase containing 36 formula units. To study similar compositions to those from experiment, the following models were simulated: $Na_{1.00}Ni_{0.5}Mn_{0.5}O_2$, $Na_{0.83}Ni_{0.5}Mn_{0.5}O_2$, $Na_{0.67}Ni_{0.5}Mn_{0.5}O_2$, $Na_{0.50}Ni_{0.5}Mn_{0.5}O_2$, $Na_{0.33}Ni_{0.5}Mn_{0.5}O_2$, $Na_{0.17}Ni_{0.5}Mn_{0.5}O_2$, $Na_{0.08}Ni_{0.5}Mn_{0.5}O_2$, $Na_{1.00}Mg_{0.11}Ni_{0.39}Mn_{0.5}O_2$, $Na_{0.83}Mg_{0.11}Ni_{0.39}Mn_{0.5}O_2$, $Na_{0.67}Mg_{0.11}Ni_{0.39}Mn_{0.5}O_2$, $Na_{0.50}Mg_{0.11}Ni_{0.39}Mn_{0.5}O_2$, $Na_{0.33}Mg_{0.11}Ni_{0.39}Mn_{0.5}O_2$, and $Na_{0.19}Mg_{0.11}Ni_{0.39}Mn_{0.5}O_2$. As the arrangements of the ions in the lattice is unknown, all possible configurations were evaluated by Coulomb interactions with the help of the so-called *supercell* code[57] assuming Na^{1+}, Mg^{2+}, and O^{2-}, and ensuring charge neutrality by oxidizing Mn^{3+} to Mn^{4+} followed by oxidation of Ni^{2+} to Ni^{3+}/Ni^{4+}. The most favorable arrangement was chosen for each structure and fully optimized without symmetry constraints by DFT calculations applying the Perdew-Burke-Ernzerhof (PBE) exchange-correlation functional.[58] The Brillouin zone was sampled by a k-point grid that includes the gamma-point and with one point at the two longest axes and 2 points at the shortest axis. The plane wave energy cutoff was set to 520 eV, and PAW potentials that treat only the valence electrons of the ions explicitly were selected. A convergence test of the cutoff energy proved that energies are converged within 4 meV per formula unit with the chosen cutoff (cf. Figure S15, Supporting Information). The geometries were optimized until the residual forces on each ion were lower than 0.02 eV $Å^{-1}$, and an electronic convergence criterion of 10^{-6} eV was employed. For the fully charged materials ($Na_{0.08}Ni_{0.5}Mn_{0.5}O_2$, $Na_{0.19}Mg_{0.11}Ni_{0.39}Mn_{0.5}O_2$), MLFF AIMD simulations[59] in an *NpT* ensemble with T = 300 K and p = 1 bar were performed. A Langevin thermostat with friction coefficients of 5 ps^{-1} for each species was employed, along with a friction coefficient of 10 ps^{-1} for the lattice together with a virtual mass of 4000 au, along with a Parinello-Rahman barostat.[60] Simulations were conducted with on-the-fly training, and trajectories of 20 ps in steps of 1 fs were obtained. Resulting evolutions of energy, temperature, and pressure are shown in Figure S16 (Supporting Information). Analysis was performed on the last 10 ps of each run (10 ps equilibration), and the lowest energy structures were again geometry optimized with the settings described above. The resulting geometries were used to further study the redox mechanisms by calculating the electronic structure with the HSE06 hybrid functional.[61] For the electronic structures, a convergence criterion of 10^{-6} eV was used. The resulting structures and spin density differences were visualized with help of the *VESTA* software package.[62] Bader charge analysis was conducted with the package of the Henkelman group[63–66] and projected densities of states were obtained with the help of vaspkit.[67] Moreover, for analysis of the MLFF AIMD runs self-written pyhton scripts were used that made use of some features of the pymatgen library.[68]

Supporting Information

Supporting Information is available from the Wiley Online Library or from the author.

Acknowledgements

Y.L. thanks the China Scholarship Council for funding (CSC No.201906240218). P.A. and K.A.M. thank the Bundesministerium für Bildung und Forschung (BMBF) for funding over project KAROFEST (03XP0498A). P.K. and P.A. acknowledge support from the German

Research Foundation (DFG, grant number 501562980). P.K. is thankful for computing time granted through JARA-HPC within project jiek12 on the supercomputer JURECA at Forschungszentrum Jülich.[69] The authors acknowledge DESY (Hamburg, Germany), a member of the Helmholtz Association HGF, for the provision of experimental facilities. Parts of this research were carried out at PETRA III. Beamtime was allocated for proposals I-20220574 and I-20211173. This work was performed using the Biologic VMP-3 potentiostat of DESY/PETRA III beamline P02.1. Y.L. and Y.S. acknowledge DESY (Hamburg, Germany), a member of the Helmholtz Association HGF, for the support with travel costs. XAS and RIXS were carried out at the KMC-2 and U41-PEAXIS beamlines, respectively, at the BESSY II electron storage ring operated by the Helmholtz-Zentrum Berlin für Materialien und Energie, GmbH. The authors thank the Helmholtz-Zentrum Berlin für Materialien und Energie, GmbH for the allocation of synchrotron radiation beamtime. The authors would like to thank Prof. Jiefang Zhu and Dr. Dan Li from the Department of Chemistry, Ångström Laboratory, Uppsala University, as well as Dr. Frederik Holm Gjørup from the DanMAX beamline for their support with operando XRD measurements (Proposal number 20241703). This publication was partly developed under the provision of the Polish Ministry and Higher Education project Support for research and development with the use of research infrastructure of the "National Synchrotron Radiation Centre SOLARIS" under contract nr 1/SOL/2021/2. The authors acknowledge the SOLARIS Center for access to the PIRX Beamline, where the measurements were performed.

Open access funding enabled and organized by Projekt DEAL.

Conflict of Interest

The authors declare no conflict of interest.

Author Contributions

Y.L. and K.K. contributed equally to this work. P.A. and Y.L. conceived the idea, Y.L. synthesized and characterized the materials, performed Rietveld refinement studies, and performed all electrochemical measurements. Operando XRD measurements were done by Y.L., K.A.M., and A.I.F. with the help of V.B. and A.S.J.M. Hard XAS experiments were performed by Y.L., K.A.M., and Y.S. with the help of G.S. Mg K-edge XAS was measured by M.Z. and Y.L. RIXS measurements were done by D.W., C.S., and Y.L. DFT calculations were done by K.K. and P.K. The data and manuscript were organized by Y.L. The manuscript was written by Y.L. and P.A. with contributions from all authors. All authors contributed to the discussion of the data analysis.

Data Availability Statement

The data that support the findings of this study are available in the supplementary material of this article.

Keywords

anionic redox, layered oxides, Mg doping, Na-ion batteries, oxygen redox, resonant inelastic X-ray scattering, sloping potential profile

Received: July 30, 2025
Revised: August 19, 2025
Published online: November 11, 2025

[1] P. K. Nayak, L. Yang, W. Brehm, P. Adelhelm, *Angew Chem Int Ed Engl* **2018**, *57*, 102.
[2] R. Usiskin, Y. Lu, J. Popovic, M. Law, P. Balaya, Y.-S. Hu, J. Maier, *Nat. Rev. Mater.* **2021**, *6*, 1020.
[3] *Sodium-Ion Batteries: Materials, Characterization and Technology*, (Eds: P. A. Maria-Magdalena Titirici, P. Adelhelm, Y.-S. Hu), Wiley, Weinheim **2022**.
[4] C. Delmas, D. Carlier, M. Guignard, *Adv. Energy Mater.* **2020**, *11*, 2001201.
[5] J. B. Goodenough, K. S. Park, *J. Am. Chem. Soc.* **2013**, *135*, 1167.
[6] W. Li, B. Song, A. Manthiram, *Chem. Soc. Rev.* **2017**, *46*, 3006.
[7] W. E. Gent, I. I. Abate, W. Yang, L. F. Nazar, W. C. Chueh, *Joule* **2020**, *4*, 1369.
[8] Y. You, A. Manthiram, *Adv. Energy Mater.* **2018**, *8*, 1701785.
[9] P.-F. Wang, Y. You, Y.-X. Yin, Y.-G. Guo, *Adv. Energy Mater.* **2018**, *8*, 1701912.
[10] N. Yabuuchi, K. Kubota, M. Dahbi, S. Komaba, *Chem. Rev.* **2014**, *114*, 11636.
[11] H. Jiang, G. Qian, R. Liu, W.-D. Liu, Y. Chen, W. Hu, *Sci. China Mater.* **2023**, *66*, 4542.
[12] W. Zuo, A. Innocenti, M. Zarrabeitia, D. Bresser, Y. Yang, S. Passerini, *Acc. Chem. Res.* **2023**, *56*, 284.
[13] R. A. House, U. Maitra, M. A. Perez-Osorio, J. G. Lozano, L. Jin, J. W. Somerville, L. C. Duda, A. Nag, A. Walters, K. J. Zhou, M. R. Roberts, P. G. Bruce, *Nature* **2020**, *577*, 502.
[14] R. A. House, G. J. Rees, K. McColl, J.-J. Marie, M. Garcia-Fernandez, A. Nag, K.-J. Zhou, S. Cassidy, B. J. Morgan, M. Saiful Islam, P. G. Bruce, *Nat. Energy* **2023**, *8*, 351.
[15] N. Yabuuchi, R. Hara, K. Kubota, J. Paulsen, S. Kumakura, S. Komaba, *J. Mater. Chem. A* **2014**, *2*, 16851.
[16] C. Zhao, Z. Yao, J. Wang, Y. Lu, X. Bai, A. Aspuru-Guzik, L. Chen, Y.-S. Hu, *Chem* **2019**, *5*, 2913.
[17] G. H. Lee, V. W. h. Lau, W. Yang, Y. M. Kang, *Adv. Energy Mater.* **2021**, *11*, 2003227.
[18] S. Komaba, N. Yabuuchi, T. Nakayama, A. Ogata, T. Ishikawa, I. Nakai, *Inorg. Chem.* **2012**, *51*, 6211.
[19] S. Chu, D. Kim, G. Choi, C. Zhang, H. Li, W. K. Pang, Y. Fan, A. M. D'Angelo, S. Guo, H. Zhou, *Angew Chem Int Ed Engl* **2023**, *62*, 202216174.
[20] K. Kubota, N. Fujitani, Y. Yoda, K. Kuroki, Y. Tokita, S. Komaba, *J. Mater. Chem. A* **2021**, *9*, 12830.
[21] S. Zheng, G. Zhong, M. J. McDonald, Z. Gong, R. Liu, W. Wen, C. Yang, Y. Yang, *J. Mater. Chem. A* **2016**, *4*, 9054.
[22] R. J. Clément, J. Xu, D. S. Middlemiss, J. Alvarado, C. Ma, Y. S. Meng, C. P. Grey, *J. Mater. Chem. A* **2017**, *5*, 4129.
[23] S. Mariyappan, T. Marchandier, F. Rabuel, A. Iadecola, G. Rousse, A. V. Morozov, A. M. Abakumov, J.-M. Tarascon, *Chem. Mater.* **2020**, *32*, 1657.
[24] Q. Wang, S. Mariyappan, J. Vergnet, A. M. Abakumov, G. Rousse, F. Rabuel, M. Chakir, J. M. Tarascon, *Adv. Energy Mater.* **2019**, *9*, 1901785.
[25] Y. Meng, J. An, L. Chen, G. Chen, L. Shi, M. Lu, D. Zhang, *Chem Commun (Camb)* **2020**, *56*, 8079.
[26] T.-Y. Yu, J. Kim, G. Oh, M. H. Alfaruqi, J.-Y. Hwang, Y.-K. Sun, *Energy Storage Mater.* **2023**, *61*, 102908.
[27] J. Ren, R. Dang, Y. Yang, K. Wu, Y. Lee, Z. Hu, X. Xiao, M. Wang, *Energy Technol.* **2020**, *8*, 1901504.
[28] K. Kubota, N. Fujitani, Y. Yoda, K. Kuroki, Y. Tokita, S. Komaba, *J. Mater. Chem. A* **2021**, *9*, 12830.
[29] K. Kubota, T. Asari, S. Komaba, *Adv. Mater.* **2023**, *35*, 2300714.
[30] H. Zhu, Z. Yao, H. Zhu, Y. Huang, J. Zhang, C. C. Li, K. M. Wiaderek, Y. Ren, C. J. Sun, H. Zhou, L. Fan, Y. Chen, H. Xia, L. Gu, S. Lan, Q. Liu, *Adv. Sci. (Weinh)* **2022**, *9*, 2200498.
[31] L. Yu, Y. X. Chang, M. Liu, Y. H. Feng, D. Si, X. Zhu, X. Z. Wang, P. F. Wang, S. Xu, *ACS Appl. Mater. Interfaces* **2023**, *15*, 23236.

[32] Y. Li, K. A. Mazzio, N. Yaqoob, Y. Sun, A. I. Freytag, D. Wong, C. Schulz, V. Baran, A. S. J. Mendez, G. Schuck, M. Zajac, P. Kaghazchi, P. Adelhelm, *Adv. Mater.* **2024**, *306*, 159.
[33] D. H. Seo, J. Lee, A. Urban, R. Malik, S. Kang, G. Ceder, *Nat. Chem.* **2016**, *8*, 692.
[34] T.-Y. Yu, J. Kim, G. Oh, M. H. Alfaruqi, J.-Y. Hwang, Y.-K. Sun, *Energy Storage Mater.* **2023**, *61*, 102908.
[35] C. Cheng, S. Li, T. Liu, Y. Xia, L. Y. Chang, Y. Yan, M. Ding, Y. Hu, J. Wu, J. Guo, L. Zhang, *ACS Appl. Mater. Interfaces* **2019**, *11*, 41304.
[36] K. Dai, J. Mao, Z. Zhuo, Y. Feng, W. Mao, G. Ai, F. Pan, Y.-d. Chuang, G. Liu, W. Yang, *Nano Energy* **2020**, *74*, 104831.
[37] I. Abate, S. Y. Kim, C. D. Pemmaraju, M. F. Toney, W. Yang, T. P. Devereaux, W. C. Chueh, L. F. Nazar, *Angew Chem Int Ed Engl* **2021**, *60*, 10880.
[38] E. Boivin, R. A. House, M. A. Pérez-Osorio, J.-J. Marie, U. Maitra, G. J. Rees, P. G. Bruce, *Joule* **2021**, *5*, 1267.
[39] X. Gao, B. Li, K. Kummer, A. Geondzhian, D. A. Aksyonov, R. Dedryvere, D. Foix, G. Rousse, M. Ben Yahia, M. L. Doublet, A. M. Abakumov, J. M. Tarascon, *Nat. Mater.* **2025**, *24*, 743.
[40] A. B. Munoz-Garcia, D. E. Bugaris, M. Pavone, J. P. Hodges, A. Huq, F. Chen, H. C. zur Loye, E. A. Carter, *J. Am. Chem. Soc.* **2012**, *134*, 6826.
[41] A. Massaro, A. B. Muñoz-García, P. P. Prosini, C. Gerbaldi, M. Pavone, *ACS Energy Lett.* **2021**, *6*, 2470.
[42] C. Zhang, R. Gao, L. Zheng, Y. Hao, X. Liu, *ACS Appl. Mater. Interfaces* **2018**, *10*, 10819.
[43] C. Zhou, L. Yang, C. Zhou, B. Lu, J. Liu, L. Ouyang, R. Hu, J. Liu, M. Zhu, *ACS Appl. Mater. Interfaces* **2019**, *11*, 7906.
[44] X. Bai, M. Sathiya, B. Mendoza-Sánchez, A. Iadecola, J. Vergnet, R. Dedryvère, M. Saubanère, A. M. Abakumov, P. Rozier, J.-M. Tarascon, *Adv. Energy Mater.* **2018**, *8*, 1802379.
[45] P.-F. Wang, Y. Xiao, N. Piao, Q.-C. Wang, X. Ji, T. Jin, Y.-J. Guo, S. Liu, T. Deng, C. Cui, L. Chen, Y.-G. Guo, X.-Q. Yang, C. Wang, *Nano Energy* **2020**, *69*, 104474.
[46] Y. Niu, Z. Hu, B. Zhang, D. Xiao, H. Mao, L. Zhou, F. Ding, Y. Liu, Y. Yang, J. Xu, W. Yin, N. Zhang, Z. Li, X. Yu, H. Hu, Y. Lu, X. Rong, J. Li, Y. S. Hu, *Adv. Energy Mater.* **2023**, *13*, 2300746.
[47] A.-C. Dippel, H.-P. Liermann, J. T. Delitz, P. Walter, H. Schulte-Schrepping, O. H. Seeck, H. Franz, *J. Synchrotron Radiat.* **2015**, *22*, 675.
[48] A. Schokel, M. Etter, A. Berghauser, A. Horst, D. Lindackers, T. A. Whittle, S. Schmid, M. Acosta, M. Knapp, H. Ehrenberg, M. Hinterstein, *J. Synchrotron Radiat.* **2021**, *28*, 146.
[49] G. Alvarez Ferrero, G. Åvall, K. A. Mazzio, Y. Son, K. Janßen, S. Risse, P. Adelhelm, *Adv. Energy Mater.* **2022**, *12*, 2202377.
[50] O. Gustafsson, A. Schökel, W. R. Brant, *Batteries Supercaps* **2021**, *4*, 1599.
[51] C. Schulz, K. Lieutenant, J. Xiao, T. Hofmann, D. Wong, K. Habicht, *J. Synchrotron Radiat.* **2020**, *27*, 238.
[52] D. M. Többens, S. Zander, *Journal of large-scale research facilities JLSRF* **2016**, *2*, A49.
[53] M. Zając, T. Giela, K. Freindl, K. Kollbek, J. Korecki, E. Madej, K. Pitala, A. Kozioł-Rachwał, M. Sikora, N. Spiridis, J. Stępień, A. Szkudlarek, M. Ślęzak, T. Ślęzak, D. Wilgocka-Ślęzak, *Nuclear Instruments and Methods in Physics Research Section B: Beam Interactions with Materials and Atoms* **2021**, *492*, 43.
[54] J. Szlachetko, J. Szade, E. Beyer, W. Błachucki, P. Ciochoń, P. Dumas, K. Freindl, G. Gazdowicz, S. Glatt, K. Guła, J. Hormes, P. Indyka, A. Klonecka, J. Kołodziej, T. Kołodziej, J. Korecki, P. Korecki, F. Kosiorowski, K. Kosowska, G. Kowalski, M. Kozak, P. Kozioł, W. Kwiatek, D. Liberda, H. Lichtenberg, E. Madej, A. Mandziak, A. Marendziak, K. Matlak, A. Maximenko, et al., *The European Physical Journal Plus* **2023**, *138*, 10.
[55] P. E. Blöchl, *Phys. Rev. B* **1994**, *50*, 17953.
[56] G. Kresse, J. Furthmüller, *Phys. Rev. B* **1996**, *54*, 11169.
[57] K. Okhotnikov, T. Charpentier, S. Cadars, *Journal of Cheminformatics* **2016**, *8*, 17.
[58] J. P. Perdew, K. Burke, M. Ernzerhof, *Phys. Rev. Lett.* **1996**, *77*, 3865.
[59] R. Jinnouchi, J. Lahnsteiner, F. Karsai, G. Kresse, M. Bokdam, *Phys. Rev. Lett.* **2019**, *122*, 225701.
[60] M. Parrinello, A. Rahman, *J. Appl. Phys.* **1981**, *52*, 7182.
[61] A. V. Krukau, O. A. Vydrov, A. F. Izmaylov, G. E. Scuseria, *J. Chem. Phys.* **2006**, *125*, 22410.
[62] K. Momma, F. Izumi, *J. Appl. Crystallogr.* **2011**, *44*, 1272.
[63] W. Tang, E. Sanville, G. Henkelman, *J Phys Condens Matter* **2009**, *21*, 084204.
[64] E. Sanville, S. D. Kenny, R. Smith, G. Henkelman, *J. Comput. Chem.* **2007**, *28*, 899.
[65] G. Henkelman, A. Arnaldsson, H. Jónsson, *Comput. Mater. Sci.* **2006**, *36*, 354.
[66] M. Yu, D. R. Trinkle, *J. Chem. Phys.* **2011**, *134*, 064111.
[67] V. Wang, N. Xu, J.-C. Liu, G. Tang, W.-T. Geng, *Comput. Phys. Commun.* **2021**, *267*, 108033.
[68] S. P. Ong, W. D. Richards, A. Jain, G. Hautier, M. Kocher, S. Cholia, D. Gunter, V. L. Chevrier, K. A. Persson, G. Ceder, *Comput. Mater. Sci.* **2013**, *68*, 314.
[69] P. Thörnig, *Journal of large-scale research facilities JLSRF* **2021**, *7*, A182.